Cytosolic Fe-superoxide dismutase safeguards *Trypanosoma cruzi* from macrophage-derived superoxide radical

Alejandra Martínez[a,b], Carolina Prolo[a,b], Damián Estrada[a,b], Natalia Rios[a,b], María Noel Alvarez[a,b], María Dolores Piñeyro[a,b,c], Carlos Robello[a,b,c], Rafael Radi[a,b,1], and Lucía Piacenza[a,b,1]

[a]Departamento de Bioquímica, Facultad de Medicina, Universidad de la República, 11800 Montevideo, Uruguay; [b]Centro de Investigaciones Biomédicas (CEINBIO), Facultad de Medicina, Universidad de la República, 11800 Montevideo, Uruguay; and [c]Laboratory of Host-Pathogen Interactions-Unidad de Biología Molecular, Institut Pasteur de Montevideo, 11800 Montevideo, Uruguay

Contributed by Rafael Radi, March 6, 2019 (sent for review December 20, 2018; reviewed by Irwin Fridovich and Christine C. Winterbourn)

Trypanosoma cruzi*, the causative agent of Chagas disease (CD), contains exclusively Fe-dependent superoxide dismutases (Fe-SODs). During *T. cruzi* invasion to macrophages, superoxide radical ($O_2^{\bullet-}$) is produced at the phagosomal compartment toward the internalized parasite via NOX-2 (gp91-*phox*) activation. In this work, *T. cruzi* cytosolic Fe-SODB overexpressers (pRIBOTEX–Fe-SODB) exhibited higher resistance to macrophage-dependent killing and enhanced intracellular proliferation compared with wild-type (WT) parasites. The higher infectivity of Fe-SODB overexpressers compared with WT parasites was lost in gp91-*phox*$^{-/-}$ macrophages, underscoring the role of $O_2^{\bullet-}$ in parasite killing. Herein, we studied the entrance of $O_2^{\bullet-}$ and its protonated form, perhydroxyl radical [($HO_2^{\bullet}$); $pK_a = 4.8$], to *T. cruzi* at the phagosome compartment. At the acidic pH values of the phagosome lumen (pH 5.3 ± 0.1), high steady-state concentrations of $O_2^{\bullet-}$ and $HO_2^{\bullet}$ were estimated (~28 and 8 μM, respectively). Phagosomal acidification was crucial for $O_2^{\bullet-}$ permeation, because inhibition of the macrophage H^+-ATPase proton pump significantly decreased $O_2^{\bullet-}$ detection in the internalized parasite. Importantly, $O_2^{\bullet-}$ detection, aconitase inactivation, and peroxynitrite generation were lower in Fe-SODB than in WT parasites exposed to external fluxes of $O_2^{\bullet-}$ or during macrophage infections. Other mechanisms of $O_2^{\bullet-}$ entrance participate at neutral pH values, because the anion channel inhibitor 5-nitro-2-(3-phenylpropylamino) benzoic acid decreased $O_2^{\bullet-}$ detection. Finally, parasitemia and tissue parasite burden in mice were higher in Fe-SODB–overexpressing parasites, supporting the role of the cytosolic $O_2^{\bullet-}$-catabolizing enzyme as a virulence factor for CD.

superoxide radical | superoxide dismutase | oxidant | *Trypanosoma cruzi* | virulence

Aerobic organisms produce superoxide radicals ($O_2^{\bullet-}$) through the one-electron reduction of molecular oxygen. Mitochondria and different isoforms of the NAD(P)H oxidases (NOXs) are among the better-known biological sources of $O_2^{\bullet-}$. Under physiological conditions, mitochondrial $O_2^{\bullet-}$ production rates are in the range of ~0.1 to 0.6 μM/s (1), increasing several fold in pathological conditions such as hyperglycemia [~6 μM/s (2)], inflammation, sepsis, and infectious processes. During phagocytosis, $O_2^{\bullet-}$ production can reach fluxes as high as 5.2 mM/s in the small volume of the neutrophil phagosome due to NADPH oxidase (NOX-2) activation (3–7). Direct and indirect toxic effects of $O_2^{\bullet-}$ have been studied since the discovery of superoxide dismutases (SODs) (EC 1.15.1.1) by McCord and Fridovich (8). The facts that these metalloenzymes are present throughout all orders of life and that the expression of the Mn-dependent mitochondrial isoform is essential for the survival of aerobic higher eukaryote organisms (9, 10) demonstrate the importance of $O_2^{\bullet-}$ detoxification. $O_2^{\bullet-}$ readily inactivates iron–sulfur-containing proteins like aconitase (11–14) via the disruption of its [4Fe–4S] cluster (15), which results in the release of free iron (16). Additionally, $O_2^{\bullet-}$ enzymatically dismutates to yield hydrogen peroxide [(H_2O_2); k_{obs} ~10^9 $M^{-1}{\cdot}s^{-1}$ at pH 7.4] (17, 18), which can either oxidize biomolecules (19), be a substrate of different enzymes (peroxiredoxins, glutathione and heme-peroxidases, and myeloperoxidase) (19, 20), or act as a signaling molecule (21, 22). However, it was not until the discovery of peroxynitrite and its potential cytotoxic effects that the mechanisms of $O_2^{\bullet-}$-mediated toxicity were better understood (23–25). Peroxynitrite is a potent one- and two-electron oxidant and nitrating species, produced by the reaction of nitric oxide ($^{\bullet}NO$) and $O_2^{\bullet-}$ at diffusion-controlled rates (~10^{10} $M^{-1}{\cdot}s^{-1}$) (26). Its biological effects are diverse, ranging from tissue oxidative damage to host immune protection toward invading pathogens (26, 27).

Chagas disease (CD), caused by the parasite *Trypanosoma cruzi*, is classified as a neglected tropical disease by the World Health Organization [(WHO); Chagas disease fact sheet (https://www.who.int/news-room/fact-sheets/detail/chagas-disease-(american-trypanosomiasis)] and is a public health concern in Latin America, with an estimated 6 to 7 million people infected and 28 million at risk, as reported by the organization in 2018. The disease is spreading worldwide as a result of migration, HIV coinfection, and organ transplantation. An estimate of ~240,000 *T. cruzi*-infected individuals currently live in the United States as of 2012 (28). *T. cruzi* is dispensed during the meal of infected triatomine bugs invading the mammalian host through skin wounds and/or mucous membranes, where they infect and proliferate in

Significance

In Chagas disease (CD), macrophages are the first line of defense against its causative agent, *Trypanosoma cruzi*. Here, we show that superoxide radical ($O_2^{\bullet-}$), a reactive species produced during phagocytosis, diffuses toward *T. cruzi*, causing toxicity. Much of $O_2^{\bullet-}$ permeation involves its protonation inside the acidic phagosome. To deal with host-derived oxidants, *T. cruzi* contains a broad antioxidant enzyme armamentarium. Herein, we generated parasites overexpressing the cytosolic superoxide dismutase (Fe-SODB) and demonstrate that this enzyme detoxifies host-derived $O_2^{\bullet-}$, preventing its toxicity. These parasites were more resistant to macrophage-dependent killing than the wild type and yielded higher parasitemias and parasite burden in heart tissue of infected mice, underscoring the role of Fe-SODB as a virulence factor for CD.

Author contributions: A.M., R.R., and L.P. designed research; A.M., C.P., D.E., and L.P. performed research; N.R., M.D.P., and C.R. contributed new reagents/analytic tools; A.M., C.P., D.E., M.N.A., R.R., and L.P. analyzed data; and A.M., R.R., and L.P. wrote the paper.

Reviewers: I.F., Duke University Medical Center; and C.C.W., University of Otago.

The authors declare no conflict of interest.

[1]To whom correspondence may be addressed. Email: rradi@fmed.edu.uy or lpiacenza@fmed.edu.uy.

This article contains supporting information online at www.pnas.org/lookup/suppl/doi:10.1073/pnas.1821487116/-/DCSupplemental.

Published online April 12, 2019.

different cell types (29, 30). To establish the infection, *T. cruzi* needs to survive the action of professional phagocytes present at the site of invasion (resident macrophages and recruited neutrophils) (6, 29, 31–36). *T. cruzi* phagocytosis disengages the assembly and activation of NOX-2 with the generation of sustained amounts of $O_2^{\bullet-}$ toward the internalized parasite (60 to 90 min) (37). A seminal work reported a role of $O_2^{\bullet-}$ in the macrophage-mediated control of *T. cruzi* infection (38). Later, it was found that $O_2^{\bullet-}$ is more toxic in immunostimulated macrophages due to its reaction with $^{\bullet}NO$ [derived from inducible nitric oxide synthase (iNOS)] to yield peroxynitrite, a potent cytotoxin against *T. cruzi* (6, 37, 39, 40). Electron microscopy images revealed the narrow space between *T. cruzi* and the macrophage phagosome membranes (37), and thus the concentrations of $O_2^{\bullet-}$ and/or peroxynitrite reached are expected to be high (4, 37). $O_2^{\bullet-}$ is a weak base and protonates to form perhydroxyl radical [$(HO_2^{\bullet})$; pK_a = 4.69 to 4.88] (41–43). Although phospholipid membranes have very low permeability to $O_2^{\bullet-}$ [2×10^{-6} cm/s (44)], both the acidic pH of the macrophage phagosome (pH 5 to 6) and the high NOX-2–derived $O_2^{\bullet-}$ micromolar concentrations in the phagosome favor the accumulation of relevant amounts of the neutral $HO_2^{\bullet}$, which could easily permeate membranes (4, 45). $HO_2^{\bullet}$ is a more potent oxidant than $O_2^{\bullet-}$ [$E^{0\prime}$ $HO_2^{\bullet}/H_2O_2$ = 1.42 V (46) and $E^{0\prime}$ $O_2^{\bullet-}/H_2O_2$ = 0.94 V (16)], being able to initiate lipid peroxidation reactions (47). $O_2^{\bullet-}$ may also enter cells through anionic channels, as described for erythrocytes (48), but the presence of these in *T. cruzi* and the ability of $O_2^{\bullet-}$ or $HO_2^{\bullet}$ to permeate parasite membranes are still not established.

T. cruzi contains four Fe-dependent SODs (Fe-SODs) located at different subcellular compartments: Fe-SODA and Fe-SODC are present in mitochondria, Fe-SODB2 is in the glycosome, and Fe-SODB is in the parasite cytosol (18, 49, 50). Parasites overexpressing Fe-SODA are more resistant to apoptosis during cardiomyocyte infections, suggesting its participation in mitochondrial-derived $O_2^{\bullet-}$ detoxification and the fine-tuning of the death-signaling process (12, 51). The interplay of Fe-SODB with cytosolic $O_2^{\bullet-}$ and its role in parasite virulence have not yet been studied. Experiments with the recombinant enzyme showed that this enzyme is more resistant to peroxynitrite-dependent enzyme inactivation than its mitochondrial counterpart (18). These observations suggest that Fe-SODB could safeguard the parasite from the oxidative challenge at the phagosome compartment.

In this work, we studied the permeation of the radicals $O_2^{\bullet-}$ and $HO_2^{\bullet}$ across the *T. cruzi* cell membrane and the role of cytosolic Fe-SODB in the modulation of host-derived $O_2^{\bullet-}$ levels and toxicity, intracellular peroxynitrite formation, and parasite virulence in vitro and in vivo.

Results

Generation of Fe-SODB–Overexpressing Parasites. To study the toxicity of macrophage-derived $O_2^{\bullet-}$ toward *T. cruzi*, we generated parasites that constitutively overexpress the cytosolic Fe-SODB (hereafter Fe-SODB parasites) (52). Fe-SODB protein expression increased with respect to wild type (WT) in both the noninfective epimastigote and infective trypomastigote stages of the parasite (Fig. 1*A*) and was localized at the parasite cytosol as shown by immunofluorescence microscopy (Fig. 1*B*). The parasite Fe-SODB concentration was estimated by Western blot, performing a calibration curve with purified *T. cruzi* recombinant enzyme (18) and the calculated epimastigote and trypomastigote cell volumes (28.1 ± 1.5 and 10.7 ± 0.7 fL, respectively) (Fig. 1 *C* and *D*). An ∼10- to 14-fold increase in enzyme concentration (corresponding to ∼2% total protein) was observed for both parasite stages (Fig. 1 *D* and *E*), resulting in an approximately sixfold increase in specific activity (∼1 to 6 U/mg), in agreement with previous reports (53). The expression of other components of the antioxidant enzyme machinery [Fe-SODA; cytosolic and mitochondrial peroxiredoxins (CPX and MPX, respectively); tryparedoxin (TXN-1 and TXN-2); and trypanothione synthetase (TS)] was not altered by the Fe-SODB overexpression (Fig. 1*E*).

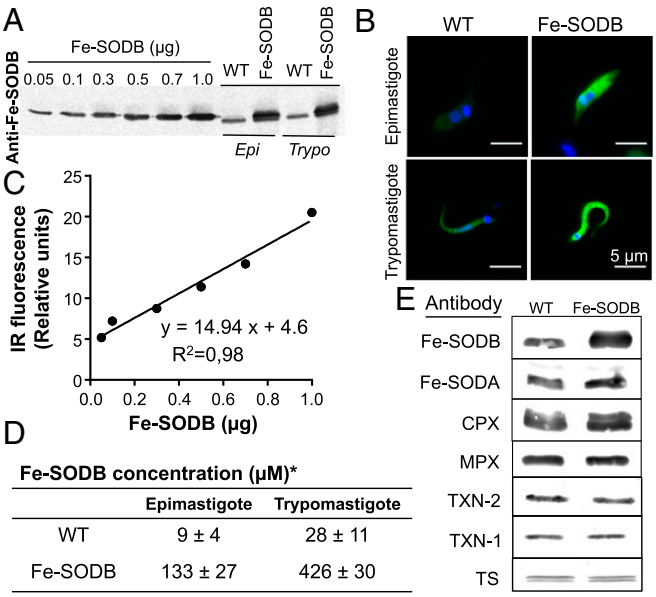

Fig. 1. Characterization of *T. cruzi* parasites overexpressing Fe-SODB. (*A*) Western blot of recombinant Fe-SODB (0.05 to 1 μg) and *T. cruzi* protein extracts (50 μg) from WT and Fe-SODB parasites using anti–Fe-SODB antibodies. Infrared (IR) images were recorded and analyzed (Image Studio). *Epi*, epimastigotes; *Trypo*, trypomastigotes. (*B*) Immunodetection of Fe-SODB in *T. cruzi* epimastigote and trypomastigotes from WT and Fe-SODB. Anti–Fe-SODB (green) and DAPI/DNA (blue). (Magnification: 400×.) (Scale bar: 5 μm.) (*C*) Data from *A* was plotted as relative IR fluorescence signal against Fe-SODB. (*D*) Calculated Fe-SODB concentration in the epimastigote and trypomastigote stage using data from *C* and the epimastigote and trypomastigote volumes (28.1 ± 1.5 and 10.7 ± 0.7 fL, respectively). Results are expressed as mean ± SEM with $n = 4$. (*E*) Western blot as above of *T. cruzi* protein extract using *T. cruzi* antibodies toward Fe-SODB, Fe-SODA, CPX, MPX, TXN-2, TXN-1, and TS.

$O_2^{\bullet-}$ Permeation Across the *T. cruzi* Plasma Membrane. To study $O_2^{\bullet-}$ permeation across the *T. cruzi* plasma membrane, we performed in vitro experiments with the xanthine/xanthine oxidase (X/XO) system as an external and controlled source of $O_2^{\bullet-}$ (54). $O_2^{\bullet-}$ detection inside *T. cruzi* was quantified using dihydroethidium (DHE)-preloaded parasites, with analytical detection of the DHE specific product 2-hydroxiethidium (2-OH-E^+) (55–57) after 40 min of incubation with a $O_2^{\bullet-}$ flux of 3 ± 0.2 μM/min at pH 7.4 (Fig. 2 *A* and *B*). An increase in 2-OH-E^+ detection in parallel with a decrease in the activity of the $O_2^{\bullet-}$-sensitive enzyme aconitase (Fig. 2 *C* and *D*) was observed for WT parasites after X/XO treatment with respect to Fe-SODB parasites. The permeability of $O_2^{\bullet-}$ in phospholipid vesicles was shown to be low [2×10^{-6} cm/s (44)], but its permeation could increase due to the presence of anion channels in the plasma membrane (48). To further evaluate the $O_2^{\bullet-}$ mechanism of permeation across *T. cruzi*, we conducted experiments (at pH 7.4) in the presence or absence of the classical anion channel inhibitor 5-nitro-2-(3-phenylpropylamino) benzoic acid (NPPB). The presence of NPPB lowered 2-OH-E^+ detection in the infective *T. cruzi* trypomastigote, supporting that, at neutral pH, $O_2^{\bullet-}$ could partially enter (∼50%) the parasite through anion channels (Fig. 2 *E* and *F*).

Macrophage-Derived $O_2^{\bullet-}$ Toxicity Toward *T. cruzi*. The direct toxicity of $O_2^{\bullet-}$ toward an internalized pathogen is difficult to determine, mainly due to the lack of specific inhibitors of NOX-2 and the generation of derived reactive species such as H_2O_2. We performed *T. cruzi* (WT and/or Fe-SODB parasites) infections to bone marrow-derived WT and/or gp91-*phox*$^{-/-}$ (NOX-2 knockout) macrophages to determine the role of $O_2^{\bullet-}$ in the control of parasite proliferation. First, Fe-SODB parasites were more infective to naïve macrophages (after 24 h), denoting the role of NOX-2–derived $O_2^{\bullet-}$ generation in

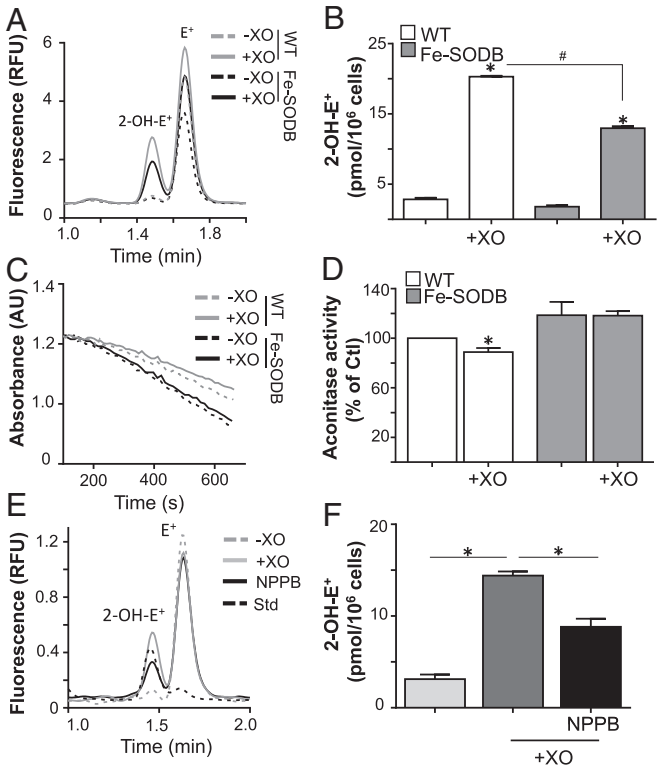

Fig. 2. $O_2^{\bullet-}$ diffusion and detection across the *T. cruzi* plasma membrane. (*A*) DHE-preloaded trypomastigote WT and/or Fe-SODB parasites (5×10^6) were incubated with xanthine (200 μM) and catalase (0.2 mg/mL) in the presence (+XO) or absence (−XO) of xanthine oxidase (50 mU/mL; $O_2^{\bullet-}$ flux = 3.1 ± 0.2 μM/min) for 40 min at 37 °C. (*B*) The amount of 2-OH-E^+ was quantified by HPLC with fluorometric detection (excitation and emission wavelengths of 510 and 567 nm, respectively). Results are expressed as picomoles of 2-OH-E^+ per 10^6 parasites and represent the mean ± SEM of four samples; $*,^{\#}P < 0.01$, two-tailed unpaired Student's *t* test. (*C* and *D*) Epimastigotes (WT and/or Fe-SODB) were incubated as in *A*, and aconitase activity was recorded at 240 nm following the decay of *cis*-aconitate (100 μM) in Tris·HCl (50 mM, pH 7.4). Activity is expressed relative to control (WT parasites) and represents the mean ± SEM of three samples; $*P < 0.05$, two-tailed unpaired Student's *t* test. (*E* and *F*) WT DHE-preloaded trypomastigotes (1×10^6) were incubated as in *A* at 37 °C. NPPB (50 μM) was added 15 min before X/XO exposure. Data represent the mean ± SEM of four samples; $*P < 0.01$. A standard mixture of 2-OH-E^+ and E^+ (Std) is shown. AU, arbitrary unit; Ctl, control; RFU, relative fluorescence unit.

cytotoxicity and parasite control (Fig. 3*A*). Second, $O_2^{\bullet-}$-dependent control of parasite proliferation was lost in gp91-*phox*$^{-/-}$ macrophages, with similar infection yields for both WT and Fe-SODB parasites (Fig. 3*A*). Importantly, Fe-SODB parasites were more infective to immunostimulated macrophages (IFN-γ/LPS) than WT parasites, suggesting its enhanced ability to detoxify intracellular $O_2^{\bullet-}$ and limiting peroxynitrite generation inside the parasite cytosol (Fig. 3*B*). The increased survival of Fe-SODB parasites with respect to WT in macrophage infections clearly supports that intraphagosomal $O_2^{\bullet-}$ is able to permeate, in significant amounts, across the *T. cruzi* plasma membrane, causing cytotoxicity either directly and/or by intracellular peroxynitrite generation.

Fe-SODB Overexpression Lowers Peroxynitrite Generation Inside the Parasite. The ability of Fe-SODB to detoxify $O_2^{\bullet-}$ inside the parasite was evaluated using fluorescein-boronate (Fl-B)-preloaded epimastigotes in the presence of 3-morpholinosydnonimine hydrochloride (SIN-1), which decomposes at physiological pH, generating similar fluxes of $O_2^{\bullet-}$ and $^{\bullet}NO$ and thus peroxynitrite (58, 59). First, SIN-1 decay (0.1 mM) was evaluated spectrophotometrically, identifying an isosbestic point at 250 nm (Fig. 4*A*). Using this wavelength, a calibration curve was performed, and the extinction coefficient determined (ε = 3,696 $M^{-1}{\cdot}cm^{-1}$; Fig. 4*A*, *Inset*). Using the absorbance at 250 nm, it was calculated that the extracellular and intracellular parasite SIN-1 concentration was the same, indicating the cell-permeant nature of the probe (Fig. 4*B*). SIN-1–derived peroxynitrite reacts with Fl-B ($k = 1.7 \times 10^6$ $M^{-1}{\cdot}s^{-1}$, at 37 °C and pH 7.4) (59); thus, in the presence of Fe-SODB, peroxynitrite generation is expected to be lower. Intracellular Fl-B oxidation was assayed by flow cytometry (10 to 30 min) in the absence or presence of SIN-1 (0.1 mM; peroxynitrite flux of ∼1.7 μM/min at 28 °C). Cytosolic Fe-SODB overexpression limits the peroxynitrite-dependent Fl-B oxidation compared with WT parasites by ∼50% at 30 min (Fig. 4 *C* and *D*). This result indicates the ability of Fe-SODB to partially prevent peroxynitrite generation due to $O_2^{\bullet-}$ detoxification, as was previously observed for *T. cruzi* mitochondrial Fe-SODA parasites (60).

Next, we evaluated the ability of Fe-SODB parasites to limit macrophage-derived peroxynitrite at the phagosome compartment. For this, macrophages were immunostimulated (IFN-γ/LPS, 5 h; iNOS induction resulting in a $^{\bullet}NO$ production rate of 0.1 to 0.2 nmol/min per 10^6 cells) and infected with Fl-B–preloaded WT and/or Fe-SODB trypomastigotes (with the consequent activation of NOX-2 and $O_2^{\bullet-}$ generation toward the internalized parasite) for 2 h (37, 38, 61, 62) (Fig. 5). Fl-B oxidation was clearly observed in the macrophage phagosome containing WT parasites, indicating peroxynitrite production as previously reported (55), while a significant decrease in probe oxidation was observed with Fe-SODB parasites, in agreement with the SIN-1 experiments (Fig. 5 *A* and *B*). Phagosome fluorescein content was evaluated by flow cytometry in the presence or absence of iNOS and NOX-2 inhibitors [10 mM Nω-nitro-L-arginine methyl ester (L-NAME) and 100 μM diphenyliodonium (DPI), respectively] (Fig. 5*C*). Intraparasite Fl-B oxidation increased several fold in immunostimulated macrophages compared with controls (Fig. 5 *B* and *C*) and was significantly decreased by L-NAME and DPI. Importantly, for the Fe-SODB parasites, the increase in Fl-B oxidation was significantly lower (Fig. 5 *B* and *C*). The difference in phagosome Fl-B oxidation between WT and Fe-SODB parasites was not due to disparity in parasite internalization, because after 2 h of infection, the invasion rate for both parasites was the same (Fig. 5*D*). The above results show that NOX-2–derived $O_2^{\bullet-}$ can permeate across the parasite membrane and, in the presence of $^{\bullet}NO$, react to form peroxynitrite at the parasite cytosol.

$O_2^{\bullet-}$ Protonation and Permeation Is Favored at Acidic pH. $O_2^{\bullet-}$ is mostly ionized at neutral pH (41) but, at the acidic pH of the phagosome, $HO_2^{\bullet}$ concentration could increase and, due to its

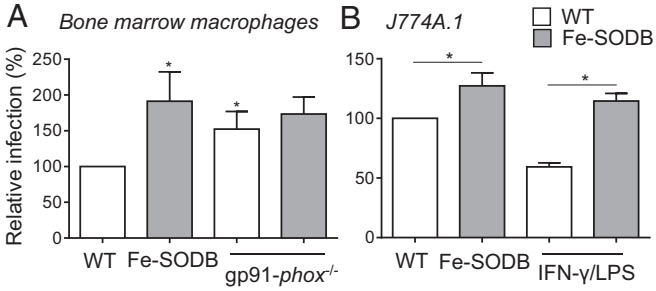

Fig. 3. Increased survival of Fe-SODB parasites in macrophage infections. (*A*) WT or gp91-*phox*$^{-/-}$ macrophages were infected with *T. cruzi* trypomastigotes (WT and/or Fe-SODB; parasite-to-macrophage ratio of 5:1) for 24 h. Infection is determined by intracellular amastigote counting (DAPI) and is expressed relative to WT parasites (100%). Data represent mean ± SEM, $n = 4$; $*P < 0.05$, two-tailed unpaired Student's *t* test. (*B*) Control and/or immunostimulated (IFN-γ/LPS) macrophages (J774A.1) were infected as in *A*. Data represent mean ± SEM, $n = 2$; $*P < 0.05$, two-tailed unpaired Student's *t* test.

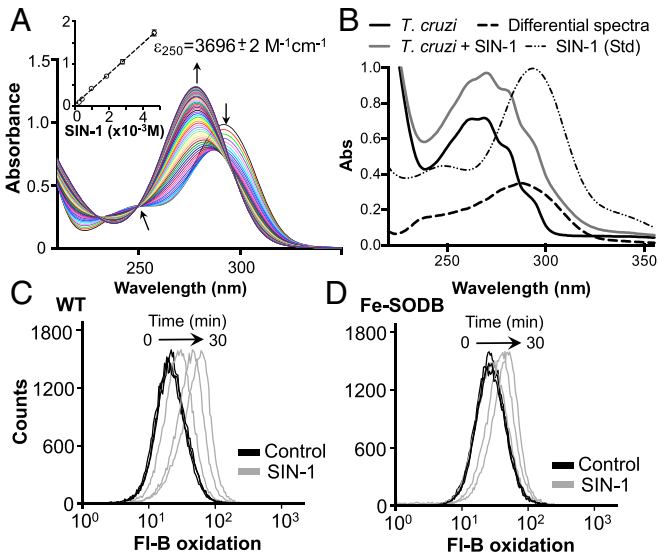

Fig. 4. Fe-SODB limits SIN-1–derived peroxynitrite generation inside the parasite. (*A*) UV-visible spectra of 0.1 mM SIN-1 [in PBS, pH 7.4, containing 0.1 mM diethylenetriamine pentaacetic acid (DTPA)] recorded at 1-min intervals. The isosbestic point at 250 nm is shown. (*Inset*) Extinction coefficient (ε) of SIN-1 (0 to 5 mM) at 250 nm. (*B*) Parasites were preloaded, or not (control), with SIN-1, and proteins were precipitated. Spectra from control and SIN-1 parasites were recorded, and the differential spectra were obtained. A spectrum from SIN-1 (0.1 mM) is shown (Std). Absorbance at 250 nm was used to estimate intracellular SIN-1 concentration (ε250 = 3,696 $M^{-1}{\cdot}cm^{-1}$). (*C* and *D*) Fl-B–preloaded epimastigotes (1×10^8) from WT (*C*) and Fe-SODB parasites (*D*) were incubated at 28 °C in dPBS in the presence or absence of 0.1 mM SIN-1. Intracellular fluorescence was analyzed by flow cytometry; arrows indicate fluorescence peak movement.

neutral charge, permeate across lipid membranes (4, 45, 63). We first experimentally determined the pH value of *T. cruzi*-containing macrophage phagosomes at early time points after phagocytosis (15 min) using fluorescein isothiocyanate (FITC)-labeled anti-*T. cruzi* antibodies in the presence or absence of the H^+-ATPase (i.e., V-ATPase) inhibitor bafilomycin A1 (B-A1) (Fig. 6). Antibodies were raised in rabbit toward a membrane-enriched *T. cruzi* fraction and labeled with the pH-sensitive probe FITC (Fig. 6*A*). FITC fluorescence decreases at acidic pH levels, allowing the estimation of pH using a calibration curve (64). The presence of B-A1 effectively blocked phagosome pH acidification, as indicated by the pH-sensitive probe pHrodo (Fig. 6*B*), and did not affect parasite internalization or macrophage NOX-2 activity (*SI Appendix*, Fig. S1). WT parasites incubated with FITC-labeled antibodies were used to infect naïve macrophages in the presence or absence of B-A1 (Fig. 6*C*). In the absence of B-A1, a dim FITC fluorescence was observed, indicating the acid pH of macrophage phagosome after *T. cruzi* internalization, whereas FITC fluorescence was evident in the presence of B-A1 (Fig. 6 *C* and *D*). Using this strategy, a standard curve was performed in macrophages infected with *T. cruzi* at controlled pH levels, and fluorescence was measured by flow cytometry (Fig. 6 *D* and *E*). Maximal fluorescence was recorded in the presence of B-A1 whereas minimal fluorescence was recorded in the absence of *T. cruzi* (Fig. 6*D*). The calculated pH for *T. cruzi*-containing phagosome was 5.3 ± 0.1 (Fig. 6*E*) and thus, under this experimental condition, ~27% of $O_2^{\bullet-}$ will be in its protonated form, $HO_2^{\bullet}$. To detect $O_2^{\bullet-}$ protonation and $HO_2^{\bullet}$ permeation toward *T. cruzi* during phagocytosis, we performed experiments with DHE-preloaded parasites and macrophages as above in the presence or absence of B-A1 and DPI. Parasite intracellular 2-OH-E^+ detection was higher in control macrophage infections and was lower in the presence of B-A1 and DPI (Fig. 6*F*). Together, these results indicate that a significant amount of $O_2^{\bullet-}$ can enter the parasite as $HO_2^{\bullet}$.

Estimation of $O_2^{\bullet-}$ and $HO_2^{\bullet}$ Steady-State Concentrations and Dynamics in the *T. cruzi*-Containing Phagosome. To study the $O_2^{\bullet-}$ and $HO_2^{\bullet}$ steady-state concentrations and dynamics in the macrophage phagosome during *T. cruzi* phagocytosis, we constructed a kinetic model considering all of the reactions and rate constants involved in $O_2^{\bullet-}$ and $HO_2^{\bullet}$ generation and consumption (Table 1). First, we calculated the rate of $O_2^{\bullet-}$ production by NOX-2 per macrophage phagosome after *T. cruzi* internalization (20 to 25 min). For this, net O_2 consumption was measured in control and in *T. cruzi*-infected WT or gp91-*phox*$^{-/-}$ macrophages (Fig. 7). The difference in O_2 consumption between *T. cruzi*-infected WT and gp91-*phox*$^{-/-}$ macrophages was considered as the O_2 consumption by NOX-2 activation, giving a value of ~2.8 nmol O_2/min per 10^6 macrophages (Fig. 7*A*). The number of phagosomes in each condition was evaluated taking into consideration the green phagosomes (FITC-labeled parasites) containing parasite DNA (Fig. 7*B*). The number of cells per condition and the number of phagosomes per macrophage (~5 phagosomes) were computed, and the net O_2 consumption rate per macrophage phagosome (R_1, Tables 1 and 2) was estimated to be $\sim 1 \times 10^{-17}$ mol/s (12 mM/s), which corresponds to ~20 mM/s $O_2^{\bullet-}$ production by NOX-2 at the phagosome lumen. The main $O_2^{\bullet-}$ and $HO_2^{\bullet}$ consumption in the phagosome lumen depends on the spontaneous dismutation. Thus, under the reactions and conditions defined in Tables 1 and 2, we

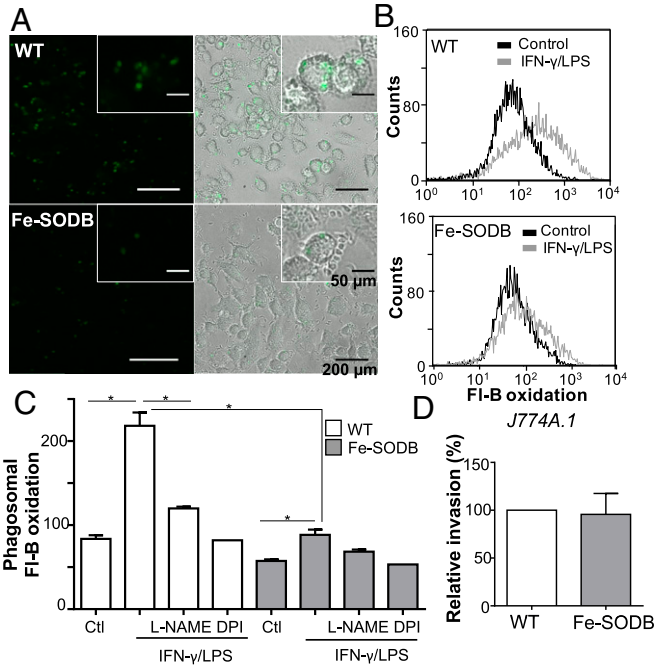

Fig. 5. Fe-SODB limits peroxynitrite generation at the phagosome. Control and/or immunostimulated (IFN-γ/LPS) macrophages (J774A.1) were infected with *T. cruzi* (WT and/or Fe-SODB; parasite-to-cell ratio of 5:1) preloaded with Fl-B in the presence or absence of 10 mM L-NAME for 2 h at 37 °C. (*A*) Fluorescence microscopy images of intraphagosomal WT and Fe-SODB parasites with oxidized Fl-B (green). Merged brightfield and fluorescence images are shown to note the intraphagosomal fluorescence localization. (Magnification: 400×.) (*B*) Flow cytometry quantification of intraparasite oxidized Fl-B in immunostimulated macrophages with respect to control. (*C*) Quantification of intraparasite Fl-B oxidation from control and immunostimulated macrophages infected with WT or Fe-SODB parasites in the presence or absence of L-NAME (10 mM) or DPI (0.1 mM). Data represent mean ± SEM of duplicates; $^*P < 0.05$, two-tailed unpaired Student's *t* test. (*D*) Invasion of WT and Fe-SODB parasites after 2 h of infection. Results are expressed relative to WT invasion (100%) and are the mean of three independent experiments.

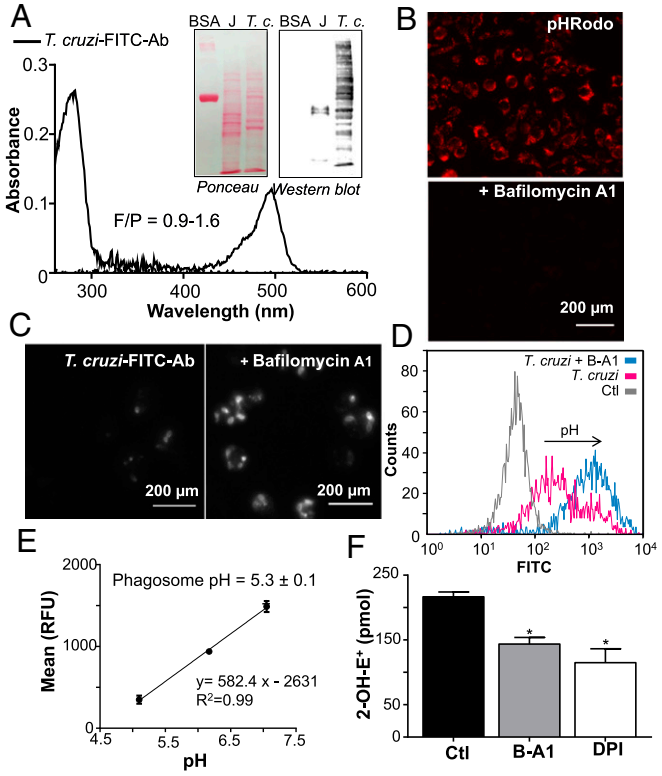

Fig. 6. Intraphagosomal pH and $O_2^{\bullet-}$ permeation toward *T. cruzi*. (*A*) Absorption spectra of the purified FITC-labeled anti-*T. cruzi* antibodies (*T. cruzi*-FITC-Ab). (*Inset*) Specificity of FITC-labeled anti-*T. cruzi* antibodies assayed by Western blot using *T. cruzi* epimastigotes (*T.c.*) and macrophage extracts (J, 50 µg). (*B*) Macrophages (J774A.1) were incubated with pHrodo-Red (100 µg/mL) in the presence or absence of B-A1, and acidic phagosomes were visualized (red spots) by fluorescence microscopy. (Magnification: 400×.) (*C*) Macrophages were infected in the presence of *T. cruzi*-FITC-Ab with or without B-A1 (0.15 µM) for 10 min at 37 °C. Noninternalized parasites were removed, and cells were incubated for 15 min at 37 °C to allow phagosome acidification. (Magnification: 400×.) Increase in FITC fluorescence is detected in B-A1–treated cultures. (*D*) Flow cytometry quantification of macrophage FITC fluorescence. B-A1 was used as positive control (maximal FITC fluorescence); arrow indicates increase in fluorescence. (*E*) Calibration curve of FITC fluorescence mean vs. pH obtained as described in *Materials and Methods*. Phagosome pH was obtained by interpolating the *T. cruzi* fluorescence mean obtained in *D* in the calibration curve. (*F*) DHE-preloaded trypomastigotes were used to infect macrophages (2 h) in the presence or absence of 0.15 µM B-A1 or 100 µM DPI, and 2-OH-E^+ was quantified by HPLC. Results are expressed as picomoles of 2-OH-E^+ per 5×10^6 macrophages and represent the mean ± SEM of three samples; $^*P < 0.05$. Ctl, control; RFU, relative fluorescence unit.

estimated steady-state concentrations in the phagosome lumen of ≤28 and ≤8 µM for $O_2^{\bullet-}$ and $HO_2^{\bullet}$, respectively, at pH 5.3. Considering the steady-state concentrations, the diffusion rate constants, and a parasite volume of ∼4 to 10 fL, the respective flux rates of $\sim 2 \times 10^{-3}$ and ∼0.2 mM/s for $O_2^{\bullet-}$ and $HO_2^{\bullet}$ were estimated. Interestingly, despite of having a smaller steady-state concentration inside the phagosome lumen, the $HO_2^{\bullet}$ influx rate is much higher than that of $O_2^{\bullet-}$ due to its higher membrane permeability. A second kinetic model was constructed to estimate $O_2^{\bullet-}$ steady-state concentrations inside the *T. cruzi* cytosol. Assuming that, at pH 5.3, the trypomastigote cytosolic pH is ∼7.1 (65), most of the $HO_2^{\bullet}$ internalized instantly deprotonates to $O_2^{\bullet-}$ [∼99.6% (41)]. Therefore, with this consideration, along with the Fe-SODB concentration presented in Fig. 1*D* and the spontaneous dismutation rate at pH 7.1, we estimated $O_2^{\bullet-}$ steady-state concentrations of ∼12 nM for the WT and 1 order of magnitude lower for *T. cruzi* Fe-SODB parasites. These values could be somewhat lower if we take into account the reactions of $O_2^{\bullet-}$ with other cellular targets, like aconitase [$k \sim 10^7$ $M^{-1} \cdot s^{-1}$ (66, 67)]. Still, knowing the concentration of Fe-SODB present in parasite cytosol and its much higher rate constant, the difference in $O_2^{\bullet-}$ steady-state concentration considering these targets is minor, and the data presented herein serve as a good approximation. Importantly, in the absence of Fe-SODB, the cytosolic $O_2^{\bullet-}$ steady-state concentration increases to ∼35 µM, indicating the central role of this enzyme in host-derived $O_2^{\bullet-}$ detoxification.

Fe-SODB Overexpression Increases Virulence in the Mouse Model of CD. For full confirmation of the enhanced virulence of the Fe-SODB parasites in vivo, we performed C57BL/6 mice infections with culture-derived trypomastigotes (Fig. 8). During the acute phase of infection, Fe-SODB parasites produced higher parasitemias (Fig. 8*A*) and higher parasite burden (three- to fourfold increase) at the heart tissue as evaluated by qPCR (Fig. 8*B*). This result, together with the above in vitro macrophage infections, underscores the relevance of the Fe-SODB content in parasite virulence.

Discussion

$O_2^{\bullet-}$ is a transient species at physiological pH due to its own dismutation [$k = 2 \times 10^5$ $M^{-1} \cdot s^{-1}$ (68)] and SOD-dependent efficient detoxification ($k \approx 10^9$) (18, 69). Indeed, the anionic nature and its low permeability to lipid membranes [2×10^{-6} cm/s (44)] confines $O_2^{\bullet-}$ mainly to its site of formation, maintaining it at very low concentrations [e.g., $\sim 10^{-10}$ to 10^{-11} M in the mitochondrial matrix (1, 2)] due to the presence of SODs. During macrophage-mediated phagocytosis and NOX-2 activation, the narrow space between the phagosomal membrane and the internalized pathogen favor a high steady-state concentration of $O_2^{\bullet-}$. In some pathogens, periplasmic and/or secreted variants of SOD may decrease $O_2^{\bullet-}$ levels in the phagocyte lumen (63, 70–72). However, in the case of *T. cruzi*, Fe-SODB is exclusively cytosolic in the early phases of phagocytosis (0 to 2 h) (18, 73). Parasites overexpressing Fe-SODB were generated to assess the toxicity of cytosolic $O_2^{\bullet-}$ toward *T. cruzi* (Fig. 1). Fe-SODB concentration in WT parasites was similar to that previously reported for mitochondrial Mn-SOD in endothelial cells (2). In Fe-SODB parasites, an increase in activity (sixfold) was observed compared with WT parasites (Fig. 1*D*). This greater content of Fe-SODB in overexpressing parasites allowed us to study its role in infections both in vitro and in vivo. First, $O_2^{\bullet-}$ permeation toward *T. cruzi* was analytically evaluated using extracellular controlled fluxes of $O_2^{\bullet-}$ (Fig. 2). The specific product of $O_2^{\bullet-}$-dependent oxidation of DHE (2-OH-E^+) was enhanced in the presence of the X/XO system, supporting $O_2^{\bullet-}$ permeation, and was significantly inhibited in Fe-SODB parasites compared with WT (Fig. 2 *A* and *B*). Aconitase is one of the cellular targets for $O_2^{\bullet-}$, leading to Fe–S cluster disruption and enzyme inactivation. A significant inhibition of total aconitase activity was observed in WT parasites (∼10%), corresponding to 25% inhibition of cytosolic activity (12), whereas no inactivation and even enhanced activity were observed

Table 1. Reactions used for assessing $O_2^{\bullet-}$ kinetics in the phagosome

Reaction	Observation*	Source
Net O_2 consumption	$R_1 = 0.012$	†
$O_2 \rightarrow O_2^{\bullet-}$	$R_2 = R_1 + (R_3 + R_4 + R_5)/2$	‡
$2O_2^{\bullet-} + 2H^+ \rightarrow O_2 + H_2O_2$	$k_3 < 0.3$–100	§
$O_2^{\bullet-} + HO_2^{\bullet} + H^+ \rightarrow O_2 + H_2O_2$	$k_4 = 8.5$–10×10^7	§
$2HO_2^{\bullet} \rightarrow O_2 + H_2O_2$	$k_5 = 7.6$–8.6×10^5	§
$O_2^{\bullet-} + H^+ \rightleftharpoons HO_2^{\bullet}$	$pK_a = 4.69$–4.88	§

*Rates (R) are in M/s. First- and second-order rate constants (k_i) are in s^{-1} and $M^{-1} \cdot s^{-1}$, respectively.
†Calculated as detailed in *Materials and Methods*.
‡The rate of NOX-2 $O_2^{\bullet-}$ production is the sum of the net O_2 consumption and half of the spontaneous dismutation rate.
§Behar et al. (41), Bielski (42), and Bielski and Allen (43).

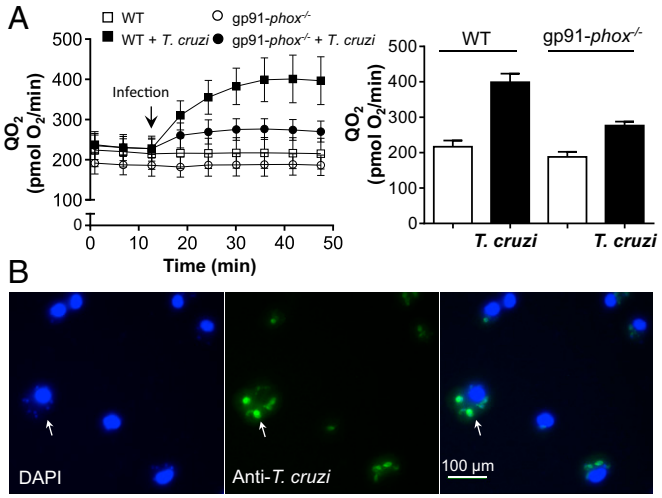

Fig. 7. Oxygen consumption and phagocytosis after *T. cruzi* infection. (*A*) O_2 consumption from WT or gp91-*phox*$^{-/-}$ macrophages were measured (Seahorse) before and after (arrow) *T. cruzi*-opsonized trypomastigote injection (parasite-to-macrophage ratio of 20:1; anti-*T. cruzi* antibody) at 37 °C (*Left*). Data at times 20 to 25 min after injection were plotted (*Right*) and represent the mean ± SEM of 10 samples. (*B*) Phagocytosis yield was evaluated by counting the number of phagosomes per cell with DAPI and FITC anti-*T cruzi* stain. (Magnification: 400×.)

in control conditions in Fe-SODB parasites, indicating the ability of Fe-SODB to detoxify $O_2^{\bullet-}$ previous to enzyme inactivation (Fig. 2 *C* and *D*). $O_2^{\bullet-}$ can permeate across the *T. cruzi* plasma membrane by the presence of anion channels detected in the parasite genome (65, 74, 75). Herein, we show that $O_2^{\bullet-}$ can use NPPB-sensitive anion channels and that their inhibition leads to a significant decrease in the intracellular 2-OH-E$^+$ detection (Fig. 2 *E* and *F*). Parasite infectivity was studied in WT and NOX-2 knockout (gp91-*phox*$^{-/-}$) macrophages; thus, no $O_2^{\bullet-}$ generation is observed during phagocytosis (Fig. 3*A*). Fe-SODB parasites were more infective to naïve macrophages than WT parasites, and this enhanced infectivity was lost in gp91-*phox*$^{-/-}$ macrophages, unequivocally demonstrating the $O_2^{\bullet-}$-dependent toxicity toward *T. cruzi* (Fig. 3*A*). Importantly, WT parasites were also more infective in gp91-*phox*$^{-/-}$ macrophages, challenging the previously proposed hypothesis of the need of an oxidative environment for parasite replication (76). Furthermore, increased infectivity of Fe-SODB parasites was also observed in immunostimulated macrophages in which both $O_2^{\bullet-}$ and $^{\bullet}NO$, and thus peroxynitrite, are generated (Fig. 3*B*). The ability of Fe-SODB to detoxify $O_2^{\bullet-}$ before peroxynitrite generation was shown in the presence of the intracellular $O_2^{\bullet-}$ and $^{\bullet}NO$ donor SIN-1 (Fig. 4) and during macrophage infections (Fig. 5). Fe-SODB parasites had significantly less peroxynitrite formation inside the parasite than WT parasites (Figs. 4 and 5). After the steady-state concentrations of $O_2^{\bullet-}$ in the phagosome lumen have been established, $^{\bullet}NO$ diffusion distances across the phagosome were estimated (77, 78). The calculations indicate that despite the high $O_2^{\bullet-}$ steady-state concentration, $^{\bullet}NO$ is still able to reach the internalized parasite, with the subsequent generation of peroxynitrite (~50% of $^{\bullet}NO$ can reach *T. cruzi* within a 100-nm distance). The harmful effects of peroxynitrite on different biomolecules are well known (27), being a highly cytotoxic molecule against *T. cruzi* (LD_{50} <0.3 fmol *T. cruzi*) (79). Interestingly, this result indicates that peroxynitrite is being produced not only inside the phagosome lumen but also inside the pathogen, and that cytosolic Fe-SODB contributes to preventing its formation by scavenging one of its precursors.

On the other hand, $O_2^{\bullet-}$ diffusion is favored by its protonation at acidic pH levels to produce the neutral radical $HO_2^{\bullet}$, which has a higher permeability coefficient than that of $O_2^{\bullet-}$ [9×10^{-4} and 2×10^{-6} cm/s (44, 63), respectively]. The rapid acidification (68, 80) of the *T. cruzi* macrophage phagosome is well known, yet the estimation of the pH at early times after invasion was needed to determine the extent of $O_2^{\bullet-}$ protonation in the phagosome compartment. Thus, we first determined the pH of the phagosome upon *T. cruzi* internalization (Fig. 6). At early times after phagocytosis (15 min), the pH of *T. cruzi*-containing phagosomes dropped from 7.1 to ~5.3, and thus in this situation, ~27% of $O_2^{\bullet-}$ will be found as $HO_2^{\bullet}$. Owing to its high permeability compared with $O_2^{\bullet-}$, the concentration at the phagosome compartment and diffusion of $HO_2^{\bullet}$ toward the internalized parasite becomes significant. In fact, previous data showed that a mutant strain of *Escherichia coli* that lacks the cytosolic and periplasmic SODs present 30% fumarase inactivation when exposed to external fluxes of $O_2^{\bullet-}$ at pH 6.5, whereas the inhibition was minimal at pH 8.4 when $HO_2^{\bullet}$ concentration is negligible (63). Interestingly, inhibition of the macrophage H^+-ATPase (i.e., phagosome acidification) decreases 2-OH-E$^+$ detection inside the phagocytized parasites, highlighting the importance of $O_2^{\bullet-}$ protonation (Fig. 6*F*). To estimate the $HO_2^{\bullet}$ concentration at the phagosome compartment, O_2 consumption and phagocytosis yield data were used to determine NOX-2 activity and $O_2^{\bullet-}$ production in individual *T. cruzi*-containing phagosomes (Fig. 7 and Table 1). Next, we constructed a model to study the kinetics and dynamics of $O_2^{\bullet-}$ and $HO_2^{\bullet}$ in the macrophage phagosome at early times of *T. cruzi* invasion (Tables 1 and 2). Steady-state concentration of $O_2^{\bullet-}$ in the phagosome was ~28 μM, within the same order of the reported value for neutrophils (7). Interestingly, despite that the steady-state concentration of $HO_2^{\bullet}$ (~8 μM) was lower than that of $O_2^{\bullet-}$, the diffusion rate toward the parasite was significantly higher due to the $HO_2^{\bullet}$ permeability coefficient, which is similar to that of H_2O_2 (2×10^{-4} to 16×10^{-4} cm/s) (7, 81, 82). However, $O_2^{\bullet-}$ permeability varies with the bilayer composition, increasing in the presence of anion channels (48). In this work, we used the $O_2^{\bullet-}$ permeability constant for phospholipid vesicles, so the diffusion rate reported herein is probably underestimated. We then simulated the steady-state concentration of $O_2^{\bullet-}$ in *T. cruzi* cytosol during phagocytosis, obtaining a value of ~12 nM for the WT and ~1 nM for Fe-SODB-overexpressing parasites. As expected, inside the phagosome, the steady-state $O_2^{\bullet-}$ concentration in the WT is 1 order of magnitude higher than the reported value for mitochondria and *E. coli* under normal conditions, ~10^{-10} to 10^{-11} M

Table 2. Conditions used for modeling $O_2^{\bullet-}$ dynamics in the phagosome

Condition	Value	Source
Phagosome lumen volume, L	8.5×10^{-16}	*
T. cruzi volume, L	3.6×10^{-15}	*
T. cruzi superficial area, cm^2	1.2×10^{-7}	*
O_2 consumed per phagosome, mol/s	1×10^{-17}	*
Phagosome pH	5.3	*
Membrane $O_2^{\bullet-}$ permeability, cm/s	2.1×10^{-6}	†
Membrane $HO_2^{\bullet}$ permeability, cm/s	9×10^{-4}	‡
$O_2^{\bullet-}$ diffusion rate constant, s^{-1}	0.3	*
$HO_2^{\bullet}$ diffusion rate constant, s^{-1}	130	*
Phagosome $O_2^{\bullet-}$ steady-state concentration, μM	28	*
Phagosome $HO_2^{\bullet}$ steady-state concentration, μM	8	*
$O_2^{\bullet-}$ diffusion rate, μM/s (mol/s)	2 (7.1×10^{-21})	*
$HO_2^{\bullet}$ diffusion rate, μM/s (mol/s)	240 (8.6×10^{-19})	*
Fe-SODB concentration, μM	28	*
Rate constant for Fe-SODB and $O_2^{\bullet-}$, $M^{-1} \cdot s^{-1}$	7.6×10^8	§

*Obtained as detailed in *Materials and Methods*.
†Takahashi and Asada (44).
‡Korshunov and Imlay (63).
§Martinez et al. (18).

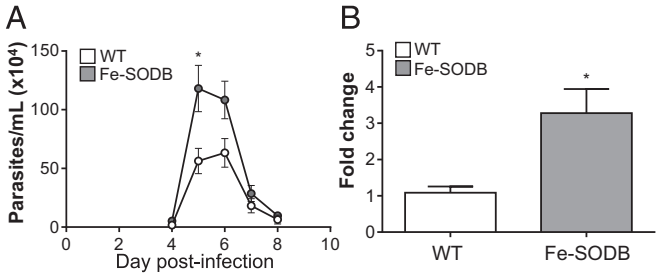

Fig. 8. Fe-SODB increases virulence in the mouse model of CD. (*A*) Mice (10 to 12 wk old) were inoculated intraperitoneally with 2×10^7 trypomastigotes, and acute infection was evaluated following parasitemia. Data represent mean ± SEM of five mice per group; $^*P < 0.05$, two-tailed unpaired Student's *t* test. (*B*) At 10 d postinfection, mice hearts were removed, and the amounts of *T. cruzi* satellite DNA and mouse chromosomal DNA (GAPDH) were quantified by qPCR. Fold change was calculated as described in *Materials and Methods*. Data represent mean ± SEM of six mice per group; $^*P < 0.01$, two-tailed unpaired Student's *t* test.

(1, 2, 83). This result highlights the importance of the presence of a robust, oxidant-resistant cytosolic Fe-SODB able to effectively detoxify $O_2^{\bullet-}$ during the macrophage oxidative assault (18). Indeed, if Fe-SODB were absent, the cytosolic $O_2^{\bullet-}$ steady-state concentration would increase to ∼35 μM, indicating the central role of this enzyme in host-derived $O_2^{\bullet-}$ detoxification. Finally, to obtain full confirmation of the enhanced virulence of the Fe-SODB-overexpressing parasites in vivo, we performed C57BL/6 mice infections (Fig. 8). Fe-SODB-overexpressing parasites produced higher parasitemias and higher parasitic burden in heart tissue at early times of infection. In Fig. 9, a schematic representation of the above-mentioned observations is shown. Together, the results presented herein show the permeation of macrophage-derived $O_2^{\bullet-}$ across the *T. cruzi* plasma membrane and the role of Fe-SODB in parasite virulence during the acute phase of CD, reflecting its function as part of the pathogen armamentarium to safeguard against host-derived cytotoxic oxidants.

Materials and Methods

Parasites and Macrophages. *T. cruzi* (Dm28c) was cultured at 28 °C as described previously (84). In vitro metacyclogenesis was performed under chemically defined conditions (85). Tissue culture-derived trypomastigotes were obtained from the supernatant of infected monolayers of Vero cells. The murine macrophage cell line J774A.1 (American Tissue Culture Collection TIB-67) was cultured at 37 °C and 5% CO_2 in DMEM (Sigma), pH 7.4, supplemented with penicillin (0.1 g/L), streptomycin (0.1 g/L), $NaHCO_3$ (1.8 g/L), and 10% heat-inactivated FBS. Primary cultures of murine bone marrow-derived macrophages were purified as described elsewhere (86) and seeded at a density of 2×10^5 cells per well in eight-well chamber slides (Nunc Lab-Tek-II). Roswell Park Memorial Institute (RPMI) medium, used to stimulate macrophage differentiation, was supplemented with 10% heat-inactivated FBS and 30% vol/vol supernatant from the L929 cell line, which secrets macrophage colony-stimulating factor. C57BL/6 WT and C57BL/6 gp91-*phox*$^{-/-}$ mice were purchased from The Jackson Laboratory (JAX stock #002365).

Generation of Fe-SODB-Overexpressing Parasites and Enzyme Concentration. Fe-SODB coding sequence was amplified and cloned in pGem-T easy vector (Promega) as described previously (18). Fe-SODB insert was obtained by digestion of pGem-T–Fe-SODB plasmid with BamHI and HindIII enzymes. The insert was purified from agarose gel and ligated (T4-DNA ligase; Fermentas) into the pRIBOTEX vector digested with the same restriction enzymes. pRIBOTEX integrates into the nuclear genome of *T. cruzi* at the ribosomal locus (52). The pRIBOTEX–Fe-SODB construct was purified from *E. coli* (XL1-blue) by alkaline lysis and sequenced. Transfection was done as described previously (87) (*SI Appendix*, for expanded *SI Materials and Methods*). Fe-SODB protein overexpression was confirmed by Western blot using specific antibody (18). To estimate Fe-SODB concentration, parasites (6×10^8 parasites per mL) were lysed (Tris·HCl, 30 mM, pH 6.8; SDS, 1% wt/vol; glycerol, 5% vol/vol; bromophenol blue, 0.005% wt/vol) and cell extracts (50 μg) or recombinant His-tagged Fe-SODB (18) (0.05 to 1 μg) was resolved by SDS/PAGE (15%), followed by Western blotting onto nitrocellulose membranes. Membranes were stained with Ponceau-S solution to evaluate protein loading and then normalized using ImageJ software. The membranes were blocked using BSA (5% wt/vol) in PBS (NaCl, 137 mM; KCl, 2.7 mM; Na_2HPO_4, 10 mM; KH_2PO_4, 2 mM) for 1 h at room temperature and probed with rabbit anti–Fe-SODB, anti–Fe-SODA, anti-MPX, anti-CPX, anti–TXN-1, anti–TXN-2, or anti-TS antibody [1:2,000 in PBS plus Tween-20 (0.1% vol/vol) and BSA (5% wt/vol)]. Immunoreactive proteins were detected using IRDye 800CW/680RD secondary antibodies (1:15,000 in PBS plus 0.1% vol/vol Tween-20), with Odyssey Infrared Imaging System (LI-COR) and analyzed with Image Studio Software. For estimation of Fe-SODB concentration (1.5×10^7 parasites), a calibration curve was performed, and Fe-SODB mass per parasite was converted to enzyme concentration using the molecular mass (ExPASy-ProtParam) tool and *T. cruzi* epimastigote and trypomastigote cell volumes (28.1 ± 1.5 and 10.7 ± 0.7 fL, respectively). Volumes were obtained from micrographs (Nikon Eclipse; 1,000×) captured from formaldehyde-fixed parasites. Cell volume results (mean ± SEM, $n = 25$) were in agreement with data using the inulin exclusion method (75).

***T. cruzi* Fe-SODB Immunocytochemistry and SOD Activity.** Parasites (1×10^8) were incubated overnight at 4 °C in fresh fixative solution (paraformaldehyde, 4% vol/vol in 0.1 M phosphate buffer, pH 7.4). Fixative was removed and cells were incubated for 15 min in permeabilization solution (PBS and Tween-20, 0.5% vol/vol) and then with rabbit anti–Fe-SODB (1:50, overnight at 4 °C) following Alexa 488-labeled anti-IgG (Invitrogen) antibody (1:1,000, 90 min). Parasite DNA was stained with DAPI (5 μg/mL) and visualized by fluorescence microscopy (Nikon Ecplise TE 200). *T. cruzi* SOD was evaluated by the cytochrome *c* (cyt *c*) reduction assay as described previously (8, 88–90). One unit of SOD activity is defined as the amount of protein necessary to inhibit 50% of cyt *c* reduction in the absence of SOD (slope ≈ 0.025 $a.u.^{-1} \cdot min^{-1}$) (91). *T. cruzi* extracts were prepared by suspending 4×10^8 epimastigotes in hypotonic lysis buffer (0.5 mL of PBS, diluted

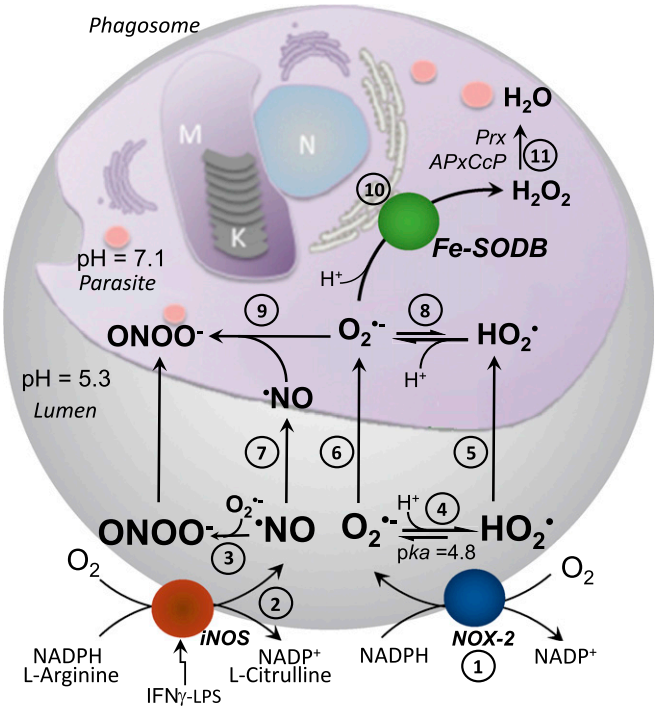

Fig. 9. Schematic representation of the reactions at the macrophage phagosome. NOX-2–derived $O_2^{\bullet-}$ (1) and iNOS-derived $^\bullet NO$ (2) are generated in the phagosome lumen with the generation of peroxynitrite ($ONOO^-$) (3). At the acidic phagosome pH (∼5.3) $O_2^{\bullet-}$ protonates to $HO_2^\bullet$ (4). $HO_2^\bullet$ can permeate (5), whereas $O_2^{\bullet-}$ enters *T. cruzi* by anion channels (6). Besides reacting with $O_2^{\bullet-}$ at the phagosome lumen, $^\bullet NO$ can also reach the parasite cytosol (7). Once in the cytosol (pH ∼ 7.1), $HO_2^\bullet$ deprotonates to $O_2^{\bullet-}$ (8), reacting intracellularly with $^\bullet NO$ to yield $ONOO^-$ (9). In the presence of Fe-SODB, $O_2^{\bullet-}$ dismutates to H_2O_2 and O_2 (10), limiting intracellular peroxynitrite generation. H_2O_2 is detoxified by parasites peroxidases (Prx, APxCcP) (11).

1:10) and lysed by five freeze–thaw cycles (1 min at 100 °C and 1 min in liquid N_2). The remaining material was centrifuged at 14,000 *g* at 4 °C for 15 min, and the supernatant was used for SOD activity. Protein content was measured by the bicinchoninic acid assay.

Exposure of Parasites to External $O_2^{\bullet-}$ Fluxes. Controlled $O_2^{\bullet-}$ fluxes were obtained by the X/XO system (200 μM and 50 mU/mL, respectively) in PBS containing catalase (0.2 mg/mL). A $O_2^{\bullet-}$ flux of ∼3.1 ± 0.2 μM/min of $O_2^{\bullet-}$ was generated as measured by the cyt *c* reduction assay at 550 nm [$\varepsilon_{550} = 2.1 \times 10^4$ $M^{-1}{\cdot}cm^{-1}$ (92)]. WT or Fe-SODB trypomastigotes (3×10^8/mL) were washed in Dulbecco's PBS (dPBS) (NaCl, 137 mM; KCl, 2.7 mM; Na_2HPO_4, 8 mM; KH_2PO_4, 1.45 mM; $CaCl_2$, 0.9 mM; $MgCl_2$, 0.5 mM; glucose, 5.5 mM; L-arginine, 1 mM) and incubated at 37 °C for 30 min with DHE (100 μM). After incubation, cells were washed with dPBS to eliminate nonincorporated probe. Preloaded DHE parasites (1×10^6 to 5×10^7, 1 mL) were incubated in PBS containing X/XO for 40 min in the presence or absence of NPPB (50 μM; Sigma) added 15 min before $O_2^{\bullet-}$ exposure. After incubation, cells were harvested, and the DHE-specific product of $O_2^{\bullet-}$ (2-OH-E^+) was quantified as described previously (55) (*SI Appendix*, for expanded *SI Materials and Methods*). DHE and DHE-derived products [2-OH-E^+ and ethidium (E^+)] were separated by HPLC with a Supelco Ascentis Express Phenyl-Hexyl column (5 cm × 4.6 mm, 2.7 μm; Sigma) equilibrated with mobile phase (65% water, 35% ACN, and 0.1% TFA). Samples were eluted isocratically (1 mL/min), and analytes monitored by fluorescence detection at 510 and 567 nm. A standard solution was prepared as described previously (93). The release of DHE and its oxidized-derived products from parasites was evaluated 2.5 h after oxidant treatment in the culture supernatant. No probe release was observed as was previously reported for this highly hydrophobic probe (55). For aconitase activity, parasites were lysed as for SOD activity and samples were centrifuged (14,000 *g*, 15 min at 4 °C). Total aconitase activity was performed in supernatants following the decay at 240 nm of *cis*-aconitate (100 μM) at 28 °C in Tris·HCl buffer (50 mM, pH 7.4). Activity is measured as the amount of *cis*-aconitate consumed per minute per milligram of epimastigote extract using the molar extinction coefficient 3.6×10^3 $M^{-1}{\cdot}cm^{-1}$. For macrophage-derived $O_2^{\bullet-}$, cells (J774A.1, 25 cm^2 confluent monolayer, $\sim 5 \times 10^6$) were infected with DHE-preloaded trypomastigotes (3×10^7) for 2 h at 37 °C in DMEM supplemented with 10% FBS. In some cases, B-A1 (0.15 μM; Sigma) or DPI (100 μM; Sigma) was added to the medium 30 min before infection to inhibit H^+-ATPase or NOX-2, respectively. The cells were harvested and centrifuged at 3,000 *g* for 5 min at room temperature. The subsequent lysis, organic extraction, and HPLC separation of the DHE-derived products was performed as above.

***T. cruzi* in Vitro Invasion and Infectivity.** Macrophages (J774A.1 and WT or gp91-*phox*$^{-/-}$) were immunostimulated (IFN-γ, 800 U/mL plus LPS, 16 μg/mL; Sigma) for 5 h before infection with *T. cruzi* trypomastigotes (61), and $^{\bullet}NO$ was measured by the Griess reagent (37, 61). After 2 h, nonengulfed parasites were removed by washing three times with PBS, and macrophages were analyzed (invasion) or further incubated for 24 h (infectivity) in DMEM plus 10% heat-inactivated FBS at 37 °C. Infected macrophages were fixed (paraformaldehyde, 4% vol/vol in PBS) for 10 min, washed, and permeabilized with Triton X-100 (0.1% vol/vol, 10 min) in PBS plus DAPI (5 μg/mL). *T. cruzi* invasion or infection (or both) was evaluated by fluorescence microscopy (1,000× magnification), and digital photographs were recorded. Infection yield at 24 h (two parasite replication rounds) was calculated as the number of amastigotes per 100 macrophages, and results were expressed as percentage (%) relative to the control condition.

Intraparasite Peroxynitrite Detection. Intracellular peroxynitrite fluxes were generated using SIN-1 (Sigma). Probe decomposition was followed by the changes in the UV spectra (1-min intervals) at 37 °C in 100 mM phosphate buffer (pH 7.4) containing 0.1 mM diethylenetriamine pentaacetic acid (DTPA). An isosbestic point at 250 nm was identified and used to determine the intraparasite SIN-1 concentration ($\varepsilon_{250} = 3{,}696$ $M^{-1}{\cdot}cm^{-1}$). Parasites (1×10^9 cells per mL; $\sim 3 \times 10^{-5}$ L) were incubated, or not, with SIN-1 (10 mM) for 10 min, and cells were collected by centrifugation (3,000 *g*, 5 min). The cell pellet was lysed, and proteins were precipitated in MeOH (1 mL) for 18 h at −20 °C. Proteins were removed by centrifugation at 20,000 *g* for 30 min, and the supernatant (intracellular SIN-1) was collected. Spectral analysis (1:5 dilution for parasite extracts) was performed, and the differential spectra from control and SIN-1 condition was recorded. The absorbance at 250 nm from the differential spectra was used to determine intracellular SIN-1 concentration. Peroxynitrite was detected using Fl-B (59). Epimastigotes (1×10^8) or culture-derived trypomastigotes (1.3×10^7) were incubated with Fl-B (100 μM) for 30 min and washed three times with dPBS. Preloaded parasites were incubated (10, 20, and 30 min) in the presence of SIN-1 (0.1 mM) at 28 °C, and intracellular fluorescence was evaluated by flow cytometry (FACSCalibur). For macrophage-derived peroxynitrite, cells (J774A.1) were incubated for 5 h with or without iNOS inducers before infection with *T. cruzi* as above. NOX-2 activation was stimulated by infection itself (37, 38, 62). DPI (100 μM) or L-NAME (10 mM; Sigma) was added to the media to inhibit NOX-2 or iNOS activity, respectively. Macrophages were infected with Fl-B–preloaded trypomastigotes (parasite-to-cell ratio of 5:1) for 2 h at 37 °C. Macrophage peroxynitrite-dependent Fl-B oxidation inside the parasite was visualized by fluorescence microscopy (400× magnification, Nikon Eclipse TE-200) and flow cytometry.

pH Determination of *T. cruzi*-Containing Phagosomes. For the determination of macrophage phagosome pH after *T. cruzi* internalization, an anti-*T. cruzi* polyclonal antibody conjugated to FITC was generated in rabbit (*SI Appendix*, for expanded *SI Materials and Methods*). Polyclonal antibodies were purified and evaluated by Western blot toward *T. cruzi* and macrophage extracts (50 μg). Purified antibodies were labeled with the pH-sensitive FITC and quantified following manufacturer instructions (Sigma). FITC-labeled antibody was used to determine the phagosome pH. Macrophages were incubated with *T. cruzi* (parasite-to-macrophage ratio of 5:1) in the presence of FITC-labeled antibody (1 mg/mL) for 10 min at 37 °C. In the absence of *T. cruzi*, no fluorescence was observed in macrophages. Noninternalized parasites were washed, and cells were further incubated in DMEM at 37 °C to allow phagosome acidification. After 15 min, medium was replaced by cold PBS plus B-A1 (0.15 μM), and the cell culture was placed on ice to stop phagosome acidification and then analyzed by fluorescence microscopy or flow cytometry. In both cases, Trypan blue (0.4% wt/vol) was added before measurements to quench extracellular fluorescence. B-A1 (0.15 μM) was used as positive control by pretreating the macrophages for 30 min. Noninfected macrophages where used as negative control. Calibration of fluorescence mean (RFU) vs. pH was obtained in situ by equilibrating the infected macrophages with cold isotonic K^+-rich medium (KCl, 140 mM; glucose, 5 mM; and citrate or phosphate salts, 15 mM) buffered with different pH values in the presence of the K^+/H^+ ionophores nigericin and valinomycin (10 μM each). Cells were incubated on ice for 5 min, allowing phagosomal pH to equilibrate with the extracellular pH, and calibration curves were constructed by plotting these values against the corresponding mean florescence. The phagosome pH was obtained by interpolating the sample fluorescence in the calibration curve. The inhibition of phagosome acidification due to B-A1 was corroborated with the pH-sensitive probe pHrodo-Red *E. coli* BioParticles Conjugate (100 μg/mL; Invitrogen). Acidic phagosomes were visualized as red spots by fluorescence microscopy. The effects of B-A1 (0.15 μM) and DPI (100 μM), added 30 min before parasite invasion, on NOX-2 activity and macrophage phagocytosis were evaluated by the nitroblue tetrazolium reduction assay (*SI Appendix*, Fig. S1) (37, 94) and by parasite invasion after 2 h of interaction as above.

Construction of a Kinetic Model at the Macrophage *T. cruzi*–Phagosome Compartment. The kinetic model of the phagosome considered that at steady-state conditions, the rate of $O_2^{\bullet-}$ and $HO_2^{\bullet}$ formation equals the rate of disappearance; that is, NOX-2 activity and $O_2^{\bullet-}$ and $HO_2^{\bullet}$ spontaneous dismutation plus their permeation toward *T. cruzi*, respectively. For the kinetic model at the parasite cytosol, we considered that the rate of $O_2^{\bullet-}$ generation is the rate of total $O_2^{\bullet-}$ and $HO_2^{\bullet}$ permeation, whereas the rate of disappearance is the Fe-SODB-dependent dismutation. Taking into account the high rate constant of $O_2^{\bullet-}$ with Fe-SODB ($k = 7.6 \pm 1.5 \times 10^8$ $M^{-1}{\cdot}s^{-1}$) (18), the contribution of other reactions has a minimal impact on $O_2^{\bullet-}$ concentration and was not considered.

Volumes and superficial areas. The phagosome, parasite volume, and superficial areas were estimated from electron micrographs of internalized parasites (1 to 2 h) (37, 80, 95), and the lumen between membranes was estimated to be ∼0.85 to 1 fL (Table 2).

O_2 consumption and phagocytosis yield. NOX-2 activity was calculated from the O_2 consumption rate. This is a net rate because O_2 is being regenerated during dismutation. Therefore, NOX-2–dependent $O_2^{\bullet-}$ formation rates in control macrophages approximately double the O_2 consumption rate. Total O_2 consumption was calculated as the difference between data of infected WT and gp91-*phox*$^{-/-}$ macrophages using a Seahorse XFe24 analyzer. Briefly, macrophages (4.5×10^4 cells per well) in DMEM (without bicarbonate) containing glutamine (2 mM), pyruvate (1 mM), Hepes (10 mM), and glucose (10 mM) were analyzed before and after *T. cruzi*-opsonized trypomastigote injection (parasite-to-macrophage ratio of 20:1, containing 1.7 mg/mL anti-*T. cruzi* antibody). Net O_2 consumption rates for *T. cruzi*-infected WT macrophages were calculated as the difference of the O_2

consumption between infected WT and gp91-*phox*$^{-/-}$ KO macrophages (20 to 25 min), reflecting NOX-2 activity after parasite internalization. Total O_2 consumption per phagosome was calculated by counting the number of phagosomes per cell by fluorescence microscopy (Nikon Eclipse TE-200) with DAPI and FITC-labeled anti-*T cruzi* stain. Because this parameter is evaluated after 20 to 25 min of invasion, it takes into account the initial changes of the phagosome pH (first 5 min) (68) and reflects the NOX-2 activity after phagosome acidification.

Spontaneous dismutation rates. Total $O_2^{\bullet-}$ spontaneous dismutation is the sum of three individual reactions (i.e., two $O_2^{\bullet-}$, two $HO_2^{\bullet}$, and one $O_2^{\bullet-}$ plus one $HO_2^{\bullet}$ molecules). For modeling the $O_2^{\bullet-}$ and $HO_2^{\bullet}$ steady-state concentrations in the phagosome (pH 5.3) and in *T. cruzi* cytosol (pH 7.1) (65), we used the three pH-independent rate constants and $O_2^{\bullet-}$ and $HO_2^{\bullet}$ pK_a values reported previously (41–43) (Table 1).

***Efflux of $O_2^{\bullet-}$ and $HO_2^{\bullet}$ from the phagosome toward* T. cruzi.** For efflux of phagosomal $O_2^{\bullet-}$ and $HO_2^{\bullet}$ toward *T. cruzi* , the following relationships hold (Eq. **1**):

$$\delta C_p/\ \delta t = k_d \times C_p = J/V_p = (P \times A/V_p) \times 10^{-3} \times (C_p - C_{tc}) = (P \times A/V_p) \times 10^{-3} \times C_p \quad [1]$$

where C_p and C_{tc} are the concentrations in the phagosome and *T. cruzi* cytosol, respectively; k_d is the diffusion rate constant; J is the flux between both compartments; V_p is the phagosome volume; A is the *T. cruzi* superficial area; and P is the permeability constant. Because $O_2^{\bullet-}$ and $HO_2^{\bullet}$ are readily consumed by the cytosolic *T. cruzi* Fe-SODB, we can ignore C_{tc}. Therefore, using the previously calculated *T. cruzi* superficial area of 1.3×10^{-7} cm^2, the phagosome lumen volume of 0.85 fL, and the membrane permeability constants of 2.1×10^{-6} cm/s (44) and 9×10^{-4} cm/s (63) for $O_2^{\bullet-}$ and $HO_2^{\bullet}$, respectively, we obtained the diffusion rate constants presented in Table 2. Finally, the influx of $O_2^{\bullet-}$ and $HO_2^{\bullet}$ (J_{in}) into *T. cruzi* and the diffusion rates ($\delta C_{tc}/\delta_t$) were calculated as follows (Eqs. **2** and **3**):

$$J_{in} = k_d \times C_{ss} \times V_p; \quad [2]$$

$$\delta C_{tc}/\ \delta_t = J_{in}/V_{tc}, \quad [3]$$

where C_{ss} is the steady-state concentration and V_{tc} is the *T. cruzi* volume. Results are shown in Table 2. $^{\bullet}$NO diffusion toward the parasite across the phagosomal lumen was estimated taking into consideration the steady-state of $O_2^{\bullet-}$ concentration (Table 2), the rate constant of $O_2^{\bullet-}$ with $^{\bullet}$NO ($k \sim 4 \times 10^9$ $M^{-1} \cdot s^{-1}$) (96), and the $^{\bullet}$NO diffusion coefficient ($D = 3 \times 10^{-5}$ cm$^2 \cdot s^{-1}$) (97) using Fick's second law as described previously (77, 78).

***T. cruzi* in Vivo Infectivity.** Female C57BL/6 mice (10 to 12 wk old) were inoculated intraperitoneally (five to six mice per group) with 2×10^7 culture-derived trypomastigotes, and acute infection was evaluated by measuring parasitemia and tissue parasite burden (by qPCR). Blood trypomastigote count was assayed on blood (3 μL) drawn from the tail tips of mice as described previously (98), and the number of trypomastigotes per 32 fields was recorded (Neubauer chamber, 400× magnification). At 10 d postinfection, the hearts (100 mg) from infected mice were recovered, washed, and homogenized in DNAzol (1 mL; Invitrogen) by using a glass homogenizer (5 to 10 strokes; Glas-Col). DNA was purified, and the amount of *T. cruzi* satellite DNA (195-bp fragment) was quantified by qPCR. Total DNA (100 ng) was analyzed on a thermal cycler with Fast SYBR Green Master Mix (Applied Biosystems) with the specific primers AATTATGAATGGCGGGAGTCA (forward) and CCAGTGTGT-GAACACGCAAAC (reverse). The amounts of mouse chromosomal DNA were quantified in parallel by qPCR using glyceraldehyde-3-phosphate dehydrogenase (GAPDH)-specific primers: CTGAGAACGGGAAGCTTGTC (forward) and CCTGCTTCACCACCTTCTTG (reverse). Each qPCR mixture (20 μL) included 2× SYBR Green SuperMix (10 μL), 0.5 μM of each primer, and DNA (100 ng). The qPCR steps were one cycle of 50 °C (10 min) and 94 °C (3 min); 40 cycles of 94 °C (45 s), 68 °C (1 min), and 72 °C (1 min); and one cycle of 72 °C (10 min). The postamplification melting curve was analyzed by measuring the fluorescence between 95 and 55 °C. Fold change was calculated as $2^{-\Delta\Delta Ct}$, where ΔCt is the difference between the Ct value of *T. cruzi* and GAPDH; and ΔΔCt is the difference between the ΔCt of Fe-SODB and WT *T. cruzi* infections.

Data Analysis and Ethics Statement for Animal Models. Data are expressed as mean ± SEM unless otherwise stated. Data were analyzed using the Student's *t* test (comparison of two groups) or one-way ANOVA (comparison of multiple groups). $P \leq 0.05$ was considered significant. All experiments were reproduced at least twice on independent days, with a minimal of three replicates each time. Animals were maintained in the facilities of Facultad de Medicina, and experiments performed in compliance with Uruguayan laws (No. 18.611) and guidelines for the use of laboratory animals (protocols "Exp. N°070153-000119-15," "Exp.N°070153-000179-13," and "071140-000880-12") approved by the Facultad de Medicina ethics committee.

ACKNOWLEDGMENTS. We thank Lic. Mariela Santos and Dr. Martín Breijo for assistance in the use of animals, Dra. Madia Trujillo for help in steady-state estimations, and Dr. Marcelo Hill for guidance in pH measurements. A.M., D.E., and N.R. were fellowship recipients from the Agencia Nacional de Investigación e Innovación. A.M., C.P., and D.E. were fellowship recipients from the Comisión Académica de Posgrado, Universidad de la República. This work was supported by the NIH Grant 1R01AI095173 and a 2015 Espacio Interdisciplinario Grant (to R.R.); by the Comisión Sectorial de Investigación Científica Grants Ini-2017-133 (to A.M.), I+D-2017 (to L.P., C.P., and M.N.A.), and Grupos 2014 (to R.R.); and by Proyecto Ley de Fundaciones (Biriden Scientific Instruments) (L.P.). Additional support was obtained from Programa de Desarrollo de Ciencias Básicas (Uruguay).

1. Cadenas E, Davies KJ (2000) Mitochondrial free radical generation, oxidative stress, and aging. *Free Radic Biol Med* 29:222–230.
2. Quijano C, Castro L, Peluffo G, Valez V, Radi R (2007) Enhanced mitochondrial superoxide in hyperglycemic endothelial cells: Direct measurements and formation of hydrogen peroxide and peroxynitrite. *Am J Physiol Heart Circ Physiol* 293:H3404–H3414.
3. Robinson JM, Badwey JA (1995) The NADPH oxidase complex of phagocytic leukocytes: A biochemical and cytochemical view. *Histochem Cell Biol* 103:163–180.
4. Winterbourn CC, Kettle AJ (2013) Redox reactions and microbial killing in the neutrophil phagosome. *Antioxid Redox Signal* 18:642–660.
5. Hirsch JG, Cohn ZA (1960) Degranulation of polymorphonuclear leucocytes following phagocytosis of microorganisms. *J Exp Med* 112:1005–1014.
6. Alvarez MN, Piacenza L, Irigoín F, Peluffo G, Radi R (2004) Macrophage-derived peroxynitrite diffusion and toxicity to Trypanosoma cruzi. *Arch Biochem Biophys* 432:222–232.
7. Winterbourn CC, Hampton MB, Livesey JH, Kettle AJ (2006) Modeling the reactions of superoxide and myeloperoxidase in the neutrophil phagosome: Implications for microbial killing. *J Biol Chem* 281:39860–39869.
8. McCord JM, Fridovich I (1969) Superoxide dismutase. An enzymic function for erythrocuprein (hemocuprein). *J Biol Chem* 244:6049–6055.
9. Li Y, et al. (1995) Dilated cardiomyopathy and neonatal lethality in mutant mice lacking manganese superoxide dismutase. *Nat Genet* 11:376–381.
10. Duttaroy A, Paul A, Kundu M, Belton A (2003) A Sod2 null mutation confers severely reduced adult life span in Drosophila. *Genetics* 165:2295–2299.
11. Andersson U, Leighton B, Young ME, Blomstrand E, Newsholme EA (1998) Inactivation of aconitase and oxoglutarate dehydrogenase in skeletal muscle in vitro by superoxide anions and/or nitric oxide. *Biochem Biophys Res Commun* 249:512–516.
12. Piacenza L, et al. (2007) Mitochondrial superoxide radicals mediate programmed cell death in Trypanosoma cruzi: Cytoprotective action of mitochondrial iron superoxide dismutase overexpression. *Biochem J* 403:323–334.
13. Irigoín F, et al. (2009) Mitochondrial calcium overload triggers complement-dependent superoxide-mediated programmed cell death in Trypanosoma cruzi. *Biochem J* 418:595–604.
14. Gardner PR, Fridovich I (1991) Superoxide sensitivity of the Escherichia coli aconitase. *J Biol Chem* 266:19328–19333.
15. Flint DH, Tuminello JF, Emptage MH (1993) The inactivation of Fe-S cluster containing hydro-lyases by superoxide. *J Biol Chem* 268:22369–22376.
16. Imlay JA (2003) Pathways of oxidative damage. *Annu Rev Microbiol* 57:395–418.
17. Sheng Y, et al. (2014) Superoxide dismutases and superoxide reductases. *Chem Rev* 114:3854–3918.
18. Martinez A, et al. (2014) Structural and molecular basis of the peroxynitrite-mediated nitration and inactivation of Trypanosoma cruzi iron-superoxide dismutases (Fe-SODs) A and B: Disparate susceptibilities due to the repair of Tyr35 radical by Cys83 in Fe-SODB through intramolecular electron transfer. *J Biol Chem* 289:12760–12778.
19. Winterbourn CC (2013) The biological chemistry of hydrogen peroxide. *Methods Enzymol* 528:3–25.
20. Klebanoff SJ, Kettle AJ, Rosen H, Winterbourn CC, Nauseef WM (2013) Myeloperoxidase: A front-line defender against phagocytosed microorganisms. *J Leukoc Biol* 93:185–198.
21. Antunes F, Brito PM (2017) Quantitative biology of hydrogen peroxide signaling. *Redox Biol* 13:1–7.
22. Sies H (2017) Hydrogen peroxide as a central redox signaling molecule in physiological oxidative stress: Oxidative eustress. *Redox Biol* 11:613–619.
23. Beckman JS, Beckman TW, Chen J, Marshall PA, Freeman BA (1990) Apparent hydroxyl radical production by peroxynitrite: Implications for endothelial injury from nitric oxide and superoxide. *Proc Natl Acad Sci USA* 87:1620–1624.
24. Radi R, Beckman JS, Bush KM, Freeman BA (1991) Peroxynitrite oxidation of sulfhydryls. The cytotoxic potential of superoxide and nitric oxide. *J Biol Chem* 266:4244–4250.
25. Radi R, Beckman JS, Bush KM, Freeman BA (1991) Peroxynitrite-induced membrane lipid peroxidation: The cytotoxic potential of superoxide and nitric oxide. *Arch Biochem Biophys* 288:481–487.
26. Ferrer-Sueta G, et al. (2018) Biochemistry of peroxynitrite and protein tyrosine nitration. *Chem Rev* 118:1338–1408.

27. Szabó C, Ischiropoulos H, Radi R (2007) Peroxynitrite: Biochemistry, pathophysiology and development of therapeutics. *Nat Rev Drug Discov* 6:662–680.
28. Bern C, Montgomery SP, Katz L, Caglioti S, Stramer SL (2008) Chagas disease and the US blood supply. *Curr Opin Infect Dis* 21:476–482.
29. Barrias ES, de Carvalho TM, De Souza W (2013) Trypanosoma cruzi: Entry into mammalian host cells and parasitophorous vacuole formation. *Front Immunol* 4:186.
30. Andrade LO, Andrews NW (2005) The Trypanosoma cruzi-host-cell interplay: Location, invasion, retention. *Nat Rev Microbiol* 3:819–823.
31. Nogueira N, Cohn Z (1976) Trypanosoma cruzi: Mechanism of entry and intracellular fate in mammalian cells. *J Exp Med* 143:1402–1420.
32. de Carvalho TM, de Souza W (1989) Early events related with the behaviour of Trypanosoma cruzi within an endocytic vacuole in mouse peritoneal macrophages. *Cell Struct Funct* 14:383–392.
33. Kierszenbaum F, Knecht E, Budzko DB, Pizzimenti MC (1974) Phagocytosis: A defense mechanism against infection with Trypanosoma cruzi. *J Immunol* 112:1839–1844.
34. Williams DM, Sawyer S, Remington JS (1976) Role of activated macrophages in resistance of mice to infection with Trypanosoma cruzi. *J Infect Dis* 134:610–623.
35. Cardoso MS, Reis-Cunha JL, Bartholomeu DC (2016) Evasion of the immune response by Trypanosoma cruzi during acute infection. *Front Immunol* 6:659.
36. Williams DM, Remington JS (1977) Effect of human monocytes and macrophages on Trypanosoma cruzi. *Immunology* 32:19–23.
37. Alvarez MN, Peluffo G, Piacenza L, Radi R (2011) Intraphagosomal peroxynitrite as a macrophage-derived cytotoxin against internalized Trypanosoma cruzi: Consequences for oxidative killing and role of microbial peroxiredoxins in infectivity. *J Biol Chem* 286:6627–6640.
38. Tanaka Y, Tanowitz H, Bloom BR (1983) Growth of Trypanosoma cruzi in a cloned macrophage cell line and in a variant defective in oxygen metabolism. *Infect Immun* 41:1322–1331.
39. Rubbo H, Denicola A, Radi R (1994) Peroxynitrite inactivates thiol-containing enzymes of Trypanosoma cruzi energetic metabolism and inhibits cell respiration. *Arch Biochem Biophys* 308:96–102.
40. Denicola A, Rubbo H, Rodríguez D, Radi R (1993) Peroxynitrite-mediated cytotoxicity to Trypanosoma cruzi. *Arch Biochem Biophys* 304:279–286.
41. Behar D, Czapski G, Rabani J, Dorfman LM, Schwarz HA (1970) Acid dissociation constant and decay kinetics of the perhydroxyl radical. *J Phys Chem* 74:3209–3213.
42. Bielski BHJ (1978) Reevaluation of the spectral and kinetic properties of HO_2 and O_2^- free radicals. *Photochem Photobiol* 28:645–649.
43. Bielski BHJ, Allen AO (1977) Mechanism of the disproportionation of superoxide radicals. *J Phys Chem* 81:1048–1050.
44. Takahashi MA, Asada K (1983) Superoxide anion permeability of phospholipid membranes and chloroplast thylakoids. *Arch Biochem Biophys* 226:558–566.
45. De Grey AD (2002) HO2*: The forgotten radical. *DNA Cell Biol* 21:251–257.
46. Ilan YA, Czapski G, Meisel D (1976) The one-electron transfer redox potentials of free radicals. I. The oxygen/superoxide system. *Biochim Biophys Acta* 430:209–224.
47. Bielski BH, Arudi RL, Sutherland MW (1983) A study of the reactivity of HO2/O2- with unsaturated fatty acids. *J Biol Chem* 258:4759–4761.
48. Lynch RE, Fridovich I (1978) Permeation of the erythrocyte stroma by superoxide radical. *J Biol Chem* 253:4697–4699.
49. Ismail SO, et al. (1997) Molecular cloning and characterization of two iron superoxide dismutase cDNAs from Trypanosoma cruzi. *Mol Biochem Parasitol* 86:187–197.
50. Temperton NJ, Wilkinson SR, Kelly JM (1996) Cloning of an Fe-superoxide dismutase gene homologue from Trypanosoma cruzi. *Mol Biochem Parasitol* 76:339–343.
51. Estrada D, et al. (2018) Cardiomyocyte diffusible redox mediators control *Trypanosoma cruzi* infection: Role of parasite mitochondrial iron superoxide dismutase. *Biochem J* 475:1235–1251.
52. Martínez-Calvillo S, López I, Hernández R (1997) pRIBOTEX expression vector: A pTEX derivative for a rapid selection of Trypanosoma cruzi transfectants. *Gene* 199:71–76.
53. Temperton NJ, Wilkinson SR, Meyer DJ, Kelly JM (1998) Overexpression of superoxide dismutase in Trypanosoma cruzi results in increased sensitivity to the trypanocidal agents gentian violet and benznidazole. *Mol Biochem Parasitol* 96:167–176.
54. McCord JM, Fridovich I (1968) The reduction of cytochrome c by milk xanthine oxidase. *J Biol Chem* 243:5753–5760.
55. Zhao H, et al. (2005) Detection and characterization of the product of hydroethidine and intracellular superoxide by HPLC and limitations of fluorescence. *Proc Natl Acad Sci USA* 102:5727–5732.
56. Zielonka J, Vasquez-Vivar J, Kalyanaraman B (2008) Detection of 2-hydroxyethidium in cellular systems: A unique marker product of superoxide and hydroethidine. *Nat Protoc* 3:8–21.
57. Zielonka J, et al. (2014) High-throughput assays for superoxide and hydrogen peroxide: Design of a screening workflow to identify inhibitors of NADPH oxidases. *J Biol Chem* 289:16176–16189.
58. Feelisch M, Ostrowski J, Noack E (1989) On the mechanism of NO release from sydnonimines. *J Cardiovasc Pharmacol* 14(Suppl 11):S13–S22.
59. Rios N, et al. (2016) Sensitive detection and estimation of cell-derived peroxynitrite fluxes using fluorescein-boronate. *Free Radic Biol Med* 101:284–295.
60. Piacenza L, Peluffo G, Alvarez MN, Martinez A, Radi R (2012) Trypanosoma cruzi antioxidant enzymes as virulence factors in Chagas disease. *Antioxid Redox Signal* 19: 723–734.
61. Alvarez MN, Trujillo M, Radi R (2002) Peroxynitrite formation from biochemical and cellular fluxes of nitric oxide and superoxide. *Methods Enzymol* 359:353–366.
62. Cardoni RL, Antunez MI, Morales C, Nantes IR (1997) Release of reactive oxygen species by phagocytic cells in response to live parasites in mice infected with Trypanosoma cruzi. *Am J Trop Med Hyg* 56:329–334.
63. Korshunov SS, Imlay JA (2002) A potential role for periplasmic superoxide dismutase in blocking the penetration of external superoxide into the cytosol of Gram-negative bacteria. *Mol Microbiol* 43:95–106.
64. Sokolovska A, Becker CE, Stuart LM (2012) Measurement of phagocytosis, phagosome acidification, and intracellular killing of Staphylococcus aureus. *Current Protoc Immunol* 99:14.30.1–14.30.12.
65. Van Der Heyden N, Docampo R (2000) Intracellular pH in mammalian stages of Trypanosoma cruzi is K+-dependent and regulated by H+-ATPases. *Mol Biochem Parasitol* 105:237–251.
66. Hausladen A, Fridovich I (1994) Superoxide and peroxynitrite inactivate aconitases, but nitric oxide does not. *J Biol Chem* 269:29405–29408.
67. Castro L, Rodriguez M, Radi R (1994) Aconitase is readily inactivated by peroxynitrite, but not by its precursor, nitric oxide. *J Biol Chem* 269:29409–29415.
68. Hackam DJ, et al. (1997) Regulation of phagosomal acidification. Differential targeting of Na+/H+ exchangers, Na+/K+-ATPases, and vacuolar-type H+-atpases. *J Biol Chem* 272:29810–29820.
69. Klug D, Rabani J, Fridovich I (1972) A direct demonstration of the catalytic action of superoxide dismutase through the use of pulse radiolysis. *J Biol Chem* 247:4839–4842.
70. Piddington DL, et al. (2001) Cu,Zn superoxide dismutase of Mycobacterium tuberculosis contributes to survival in activated macrophages that are generating an oxidative burst. *Infect Immun* 69:4980–4987.
71. Fang FC, et al. (1999) Virulent Salmonella typhimurium has two periplasmic Cu, Zn-superoxide dismutases. *Proc Natl Acad Sci USA* 96:7502–7507.
72. De Groote MA, et al. (1997) Periplasmic superoxide dismutase protects Salmonella from products of phagocyte NADPH-oxidase and nitric oxide synthase. *Proc Natl Acad Sci USA* 94:13997–14001.
73. Mateo H, Marín C, Pérez-Cordón G, Sánchez-Moreno M (2008) Purification and biochemical characterization of four iron superoxide dismutases in Trypanosoma cruzi. *Mem Inst Oswaldo Cruz* 103:271–276.
74. Grisard EC, et al. (2014) Trypanosoma cruzi clone Dm28c draft genome sequence. *Genome Announc* 2:e01114-13.
75. Rohloff P, Rodrigues CO, Docampo R (2003) Regulatory volume decrease in Trypanosoma cruzi involves amino acid efflux and changes in intracellular calcium. *Mol Biochem Parasitol* 126:219–230.
76. Paiva CN, et al. (2012) Oxidative stress fuels Trypanosoma cruzi infection in mice. *J Clin Invest* 122:2531–2542.
77. Romero N, Denicola A, Souza JM, Radi R (1999) Diffusion of peroxynitrite in the presence of carbon dioxide. *Arch Biochem Biophys* 368:23–30.
78. Lancaster JR, Jr (1994) Simulation of the diffusion and reaction of endogenously produced nitric oxide. *Proc Natl Acad Sci USA* 91:8137–8141.
79. Piacenza L, Alvarez MN, Peluffo G, Radi R (2009) Fighting the oxidative assault: The Trypanosoma cruzi journey to infection. *Curr Opin Microbiol* 12:415–421.
80. Ley V, Robbins ES, Nussenzweig V, Andrews NW (1990) The exit of Trypanosoma cruzi from the phagosome is inhibited by raising the pH of acidic compartments. *J Exp Med* 171:401–413.
81. Seaver LC, Imlay JA (2001) Hydrogen peroxide fluxes and compartmentalization inside growing Escherichia coli. *J Bacteriol* 183:7182–7189.
82. Antunes F, Cadenas E (2000) Estimation of H2O2 gradients across biomembranes. *FEBS Lett* 475:121–126.
83. Imlay JA, Fridovich I (1991) Assay of metabolic superoxide production in Escherichia coli. *J Biol Chem* 266:6957–6965.
84. Piacenza L, Peluffo G, Radi R (2001) L-arginine-dependent suppression of apoptosis in Trypanosoma cruzi: Contribution of the nitric oxide and polyamine pathways. *Proc Natl Acad Sci USA* 98:7301–7306.
85. Bonaldo MC, Souto-Padron T, de Souza W, Goldenberg S (1988) Cell-substrate adhesion during Trypanosoma cruzi differentiation. *J Cell Biol* 106:1349–1358.
86. Choi KD, Vodyanik M, Slukvin II (2011) Hematopoietic differentiation and production of mature myeloid cells from human pluripotent stem cells. *Nat Protoc* 6:296–313.
87. Piñeyro MD, Parodi-Talice A, Arcari T, Robello C (2008) Peroxiredoxins from Trypanosoma cruzi: Virulence factors and drug targets for treatment of Chagas disease? *Gene* 408:45–50.
88. Flohé L, Otting F (1984) Superoxide dismutase assays. *Methods Enzymol* 105:93–104.
89. Crapo JD, McCord JM, Fridovich I (1978) Preparation and assay of superoxide dismutases. *Methods Enzymol* 53:382–393.
90. Beyer WF, Jr, Fridovich I (1987) Assaying for superoxide dismutase activity: Some large consequences of minor changes in conditions. *Anal Biochem* 161:559–566.
91. Alvarez B, et al. (2004) Inactivation of human Cu,Zn superoxide dismutase by peroxynitrite and formation of histidinyl radical. *Free Radic Biol Med* 37:813–822.
92. Massey V (1959) The microestimation of succinate and the extinction coefficient of cytochrome c. *Biochim Biophys Acta* 34:255–256.
93. Zielonka J, Zhao H, Xu Y, Kalyanaraman B (2005) Mechanistic similarities between oxidation of hydroethidine by Fremy's salt and superoxide: Stopped-flow optical and EPR studies. *Free Radic Biol Med* 39:853–863.
94. Baehner RL, Boxer LA, Davis J (1976) The biochemical basis of nitroblue tetrazolium reduction in normal human and chronic granulomatous disease polymorphonuclear leukocytes. *Blood* 48:309–313.
95. Villalta F, Kierszenbaum F (1984) Role of inflammatory cells in Chagas' disease. II. Interactions of mouse macrophages and human monocytes with intracellular forms of Trypanosoma cruzi: Uptake and mechanism of destruction. *J Immunol* 133: 3338–3343.
96. Goldstein S, Czapski G (1995) The reaction of NO. with O2.– and HO2.: A pulse radiolysis study. *Free Radic Biol Med* 19:505–510.
97. Zacharia IG, Deen WM (2005) Diffusivity and solubility of nitric oxide in water and saline. *Ann Biomed Eng* 33:214–222.
98. Araújo-Jorge TC, de Castro SL (2000) *Doença de Chagas: Manual Para Experimentação Animal* (Editora FIOCRUZ, Rio de Janeiro).